RESEARCH ARTICLE

WILEY

Frequency converting and digital modulation of light derived from lanthanide for signal encoding and logic computing

Haisheng Chen[1] | Jiaying Shen[2] | Xiaona Du[3] | Songhua Cai[4] | Feng Guo[4,5] | Weng Fu Io[4] | Tianhong Zhou[1] | Zhengang Dong[2] | Taiyu Bian[1] | Jiaxing Guo[1] | Weiwei Liu[1] | Yang Zhang[1] | Zhenping Wu[2] | Jianhua Hao[4,5]

[1]Institute of Modern Optics and Tianjin Key Laboratory of Micro-Scale Optical Information Science and Technology, Nankai University, Tianjin, the People's Republic of China

[2]State Key Laboratory of Information Photonics and Optical Communications & School of Science, Beijing University of Posts and Telecommunications, Beijing, the People's Republic of China

[3]Institute of Photoelectric Thin Film Devices and Technology, College of Electronic Information and Optical Engineering, Nankai University, Tianjin, the People's Republic of China

[4]Department of Applied Physics, The Hong Kong Polytechnic University, Hung Hom, Hong Kong, the People's Republic of China

[5]The Hong Kong Polytechnic University Shenzhen Research Institute, Shenzhen, the People's Republic of China

Correspondence
Yang Zhang, Institute of Modern Optics and Tianjin Key Laboratory of Micro-Scale Optical Information Science and Technology, Nankai University, Tianjin 300071, the People's Republic of China.
Email: yangzhang@nankai.edu.cn

Zhenping Wu, State Key Laboratory of Information Photonics and Optical Communications & School of Science, Beijing University of Posts and Telecommunications, Beijing 100876, the People's Republic of China.
Email: zhenpingwu@bupt.edu.cn

Jianhua Hao, Department of Applied Physics, The Hong Kong Polytechnic University, Hung Hom, Hong Kong, the People's Republic of China.
Email: jh.hao@polyu.edu.hk

Abstract

Modulation of light underpins a central part of modern optoelectronics. Conventional optical modulators based on refractive-index and absorption variation in the presence of an electric field serve as the workhorse for diverse photonic technologies. However, these approaches based on electro-refraction or electro-absorption effect impose limitations on frequency converting and signal amplification. Lanthanide-activated phosphors offer a promising platform for nonlinear frequency conversion with an abundant spectrum. Here, we propose a novel approach to achieve frequency conversion and digital modulation of light signal by coupling lanthanide luminescence with an electrically responsive ferroelectric host. The technological benefits of such paradigm-shifting solution are highlighted by demonstrating a quasi-continuous and enhancement of the lanthanide luminescence. The ability to locally manipulate light emission can convert digital information signals into visible waveforms, and visualize electrical logic and arithmetic operations. The proof-of-concept device exhibits perspectives for developing light-compatible logic functions. These results pave the way to design more controllable lanthanide photonics with desired opto-electronic coupling.

1 | INTRODUCTION

Light modulators, devices that can manipulate the irradiance or direction of light, are essential for optoelectronics and diverse photonic technologies. They can be categorized into different types depending on the mechanism of modulation, such as electro-optic, magneto-optic, or acousto-optic modulators.[1–5] Among all optical-field parameters, amplitude modulation is the most common form since the simplicity of envelope photodetection.[6] The current state-of-the-art technology relies on electrically varying the optical susceptibility of the modulator material, which can be either refractive or absorptive modulation depending on whether the real or imaginary part of the susceptibility is modulated. Recently, light-based information processing and computing are continuing to pave the path forward to fulfill the ever-increasing demand.[7–9] Optical modulators for electro-refraction or electro-absorption have dramatically improved performance. Furthermore, light modulators with frequency conversion and signal amplification allow for leveraging even more computational capabilities. To date, frequency conversion in nonlinear crystals such as difference-frequency generation, sum-frequency generation, and second-harmonic generation can only emit light beams with specific wavelengths, and often have low efficiency.[10–12] Lanthanide-doped phosphors represent an attractive alternative as frequency-converter, which are capable of emitting downconversion or upconversion luminescence covering the visible to near-infrared region.[13–17] Lanthanide-based light modulator would provide a promising route to develop paradigm-shifting hardware architectures.

Lanthanide ions occupy an important position in emerging information photonics due to their unique photophysical properties, especially involving the generation and amplification of light.[18–22] In particular, harnessing lanthanide dopants' long-lived coherence and stable optical transitions enables a solid-state quantum memory of photonic entanglement for quantum communication and computing.[23,24] The ability of controlling, manipulating, and encoding the light derived from the lanthanide is the prerequisite for the development of lanthanide-activated optical modulation technologies. Temporal modulations have been realized via varying excitation wavelengths or pulse width,[25,26] which need to face rigorous issues related to sophisticated laser systems. Implementations of strain and thermal fields suffer from limitations associated with device integration and modulation rate.[27–29] Electric field represents the most effective and convenient tuning knob in consideration of the controllability and mature microelectronic technology. The most studied light derived from the lanthanide arises from electric dipole transitions within the 4f configuration of trivalent lanthanide ions (Ln^{3+}), which are shielded from the surroundings by the filled $5s^2$ and $5p^6$ subshells. While, the host materials exert a strong influence on the emission efficiency and profile.[30] In most cases, the electrical control strategies seek to impact on the hosts rather than on the lanthanide ions. Applying an electric field to some kinds of electro-responsive materials, such as liquid crystal polymer,[31] electrochromic molecules,[32] causes either electro-refraction or electro-absorption effect interacting with the generated luminescence, resulting in a desired manipulation. Apparently, these "passive" modulations tend to linearly shunt or limit the lanthanide emissions. Whereas, modulation can be also realized by electrically controlling optical emissions through surrounding crystal/ligand field variation,[33] or reactions of lanthanide dopants.[34] As an "active" method, an electric field can influence the 4f transition probabilities or long-lived hyperfine states of dopant ions in an either direct or indirect way, leading to an expected amplification of lanthanide luminescence.

The unique crystal structure of perovskite oxide ferroelectrics provides an opportunity to couple variables including electric field and strain to crystal symmetry in a single compound. Defect and interface engineering offers an extra degree of freedom not only for ameliorating physical properties but also for delivering additional functionalities. In ferroelectric oxides, electrically induced migration and accumulation of point defect would alter the band diagram and local structural symmetry at the interface.[35] Thus, lanthanide-doped ferroelectrics provide us a platform to investigate the active modulation of lanthanide luminescence. The coupling between the introduced controllable lanthanide luminescence and intrinsic properties existing in ferroelectric hosts could give rise to unprecedented device characteristics. Previous studies have proven the feasibility of electric-induced enhancement and modulation of luminescence in lanthanide-doped ferroelectrics.[36,37]

However, the kinetic process and frequency response of the modulation have been barely reported, not to mention the related prototype devices. Here we demonstrate electrical modulation of light derived from lanthanide Er^{3+}-activated ferroelectric films via local application of electric field. Er^{3+} ion was chosen in consideration of its superior luminescent properties as well as the broad applications. The prominent feature of such design is that the lanthanide light emission can be continuously enhanced with an external electric field. We can encode a digital information signal into the amplitude of the lanthanide luminescence. The proof-of-concept device exhibits perspectives for light-compatible logic functions.

2 | RESULTS AND DISCUSSION

2.1 | Device fabrication and characterizations

First, we prepared epitaxial BTO:Er thin films on (001) Nb:SrTiO$_3$ (NSTO, Nb:0.7 wt%) substrates via pulsed laser deposition (PLD). Figure 1A shows θ–2θ x-ray diffraction (XRD) spectrum of the BTO:Er/NSTO heterostructure, which reveals epitaxy of (001) perovskite phase with no detectable secondary phase. Azimuthal ϕ scans in Figure S1 confirm in-plane cube-on-cube epitaxial relationship of [100] BTO//[100] NSTO. A further high-
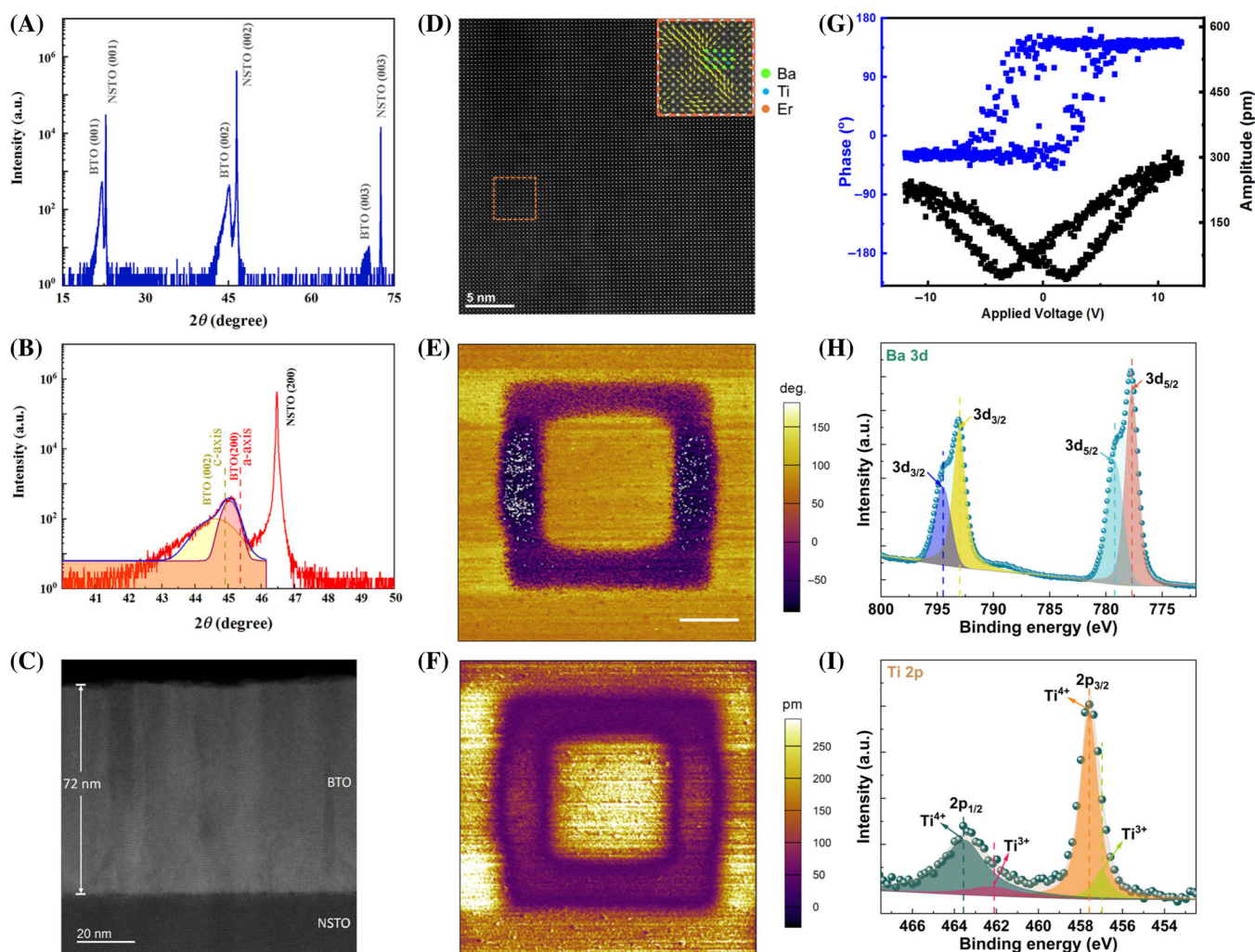

FIGURE 1 Characterizations of BTO:Er thin film on a conductive NSTO substrate. (A) XRD pattern confirms epitaxial growth of BTO:Er thin film. (B) High-resolution diffraction around BTO (002) peak shows the presence of the *a*-axis and *c*-axis domains. (C) Low-magnification high-resolution cross-sectional HAADF-STEM image of the BTO:Er thin film grown on NSTO substrate. (D) An atomically resolved HAADF-STEM image of the BTO:Er thin film. The inset shows the substitution places of Er doping ions overlaid with polarization vectors. (E) PFM out-of-plane phase of as-grown BTO:Er thin film. (F) PFM amplitude images of domain switching results for as-grown BTO:Er thin film. (G) Local PFM hysteresis loops. (H,I) The high-resolution XPS spectra of Ba 3d and Ti 2p in the BTO:Er thin film, respectively.

resolution XRD around the (002) BTO:Er peak demonstrates the presence of the *a*-axis domains along with the *c*-axis domains in the as-grown BTO:Er thin film (Figure 1B). Figure 1C is a cross-sectional TEM image of the BTO:Er/NSTO heterostructure, in which the uniform and well-defined interface could minimize the interfacial defects/dislocations. The high-angle annular dark-field scanning transmission electron microscopy (HAADF-STEM) image shown in Figure 1D exhibits the high crystalline quality in BTO:Er films, and the epitaxial alignment between the layers. Atomically resolved cross-sectional HAADF-STEM image confirms that the Er dopants occupy the B-site of the crystal lattice. The inset in Figure 1D shows the calculated polarization vectors overlaid with the image. The spontaneous polarization of BTO:Er film is relatively small, whereas some nanodomains exhibit large polarization magnitude that may result from Er doping. High-resolution HAADF-STEM image overlaid with vectors in Figure S2 demonstrates the coexistence of the in-plane polar state (*a*-axis domain) and out-of-plane polar state (*c*-axis domain). Figure 1E,F show the out-of-plane piezoresponse force microscopy (PFM) phase and amplitude images of ferroelectric domains written on the BTO:Er with $\pm$10 V. The antiparallel polarization with 180° phase contrast can be maintained for hours. PFM hysteresis loops in Figure 1G confirm the ferroelectric nature of the BTO:Er thin film, and the minima of the amplitude and phase loops reveal that the local coercive voltages are about +2.2 V and −3.8 V. Furthermore, we performed x-ray photoelectron spectroscopy (XPS) to characterize the valence states of elements in BTO:Er film (Figure S3). The high-resolution XPS spectra in Figure 1H can be well fitted into two overlapping spin-orbit-split pairs (Ba $3d_{3/2}$ and Ba $3d_{5/2}$), indicating Ba^{2+} state in the BTO:Er film. The Ti 2p spectra in Figure 1I can be deconvoluted into four Gaussian peaks, two main peaks located at 457.6 and 463.6 eV, corresponding to the Ti $2p_{3/2}$ and Ti $2p_{1/2}$ peaks of Ti^{4+} in BTO:Er. Likewise, two smaller additional peaks at 457.0 and 462.2 eV can be assigned to the binding states of Ti^{3+} ions, suggesting the presence of small amount of Ti^{3+} ions in BTO:Er film.

2.2 | Modulation of light emission

Figure 2A schematically depicts the device made of ITO/BTO:Er/NSTO heterostructure. The time-integrated light emission of the BTO:Er film as a function of DC bias is shown in Figure 2B. For the sake of a better exhibition, the contour map of PL spectra under different DC bias is given in Figure 2C. Under 980 nm diode laser excitation, green emission bands located at 527 and 551 nm

correspond to $^2H_{11/2}/^4S_{3/2} \rightarrow ^4I_{15/2}$ transitions of Er^{3+}, while red emission band at 658 nm can be attributed to the $^4F_{9/2} \rightarrow ^4I_{15/2}$ transition of Er^{3+} (Figure S4). The pump power *P* dependence of upconversion intensity *I* is shown in Figure S5, indicating two-photon process is involved for both green and red emissions. Thus, through upconversion frequency converting process, Er^{3+} ions transform near-infrared wavelength excitation into visible green and red emissions. Moreover, taking into consideration the fluorescent intensity ratio of two thermally linked energy levels of Er^{3+} ion, that is, $^2H_{11/2}$ and $^4S_{3/2}$, can reflect the temperature of the as-grown BTO:Er film well, we demonstrated the I_{527}/I_{551} value as a function of the excitation power in Figure S6, where I_{527} and I_{551} denote the emitting intensity at the wavelengths of 527 and 551 nm. The neglected fluctuation of I_{527}/I_{551} values around 0.38 as shown in Figure S6 unambiguously indicate that there is no evident variation in the temperature of the as-grown BTO:Er film, which rules out the heating effect induced by 980 nm laser. When we apply the DC bias on the BTO:Er thin film, the photoluminescence (PL) intensities for both green and red bands demonstrate obvious increases. Figure 2D shows the PL enhancement factors versus the applied voltage. It can be found that the enhancement factor for emissions at 551 nm reaches up to 2.04. And the intensity ratio of green to red emission ($f_{g/r}$) also increases with the voltage. A potential application of this method is that the emission color could be modulated under electric field by tailoring the intensity ratio of different emission bands. The in situ PL enhancement is believed to stem from the electric-induced increment of the radiative transition probabilities, which is verified by the variation of PL lifetime with and without DC bias. As shown in Figure 2E, the lifetime at 551 nm reduces from 59.6 to 44.5 µs when the voltage increases from 0 to 10 V. The measured lifetime (τ) can be calculated by: $1/\tau = W_R + W_{NR} + W_{ET}$, where W_R is the radiative rate, W_{NR} and W_{ET} are the non-radiative rate and energy transfer rate, respectively. Since the influence of electric field on the non-radiative rate and energy transfer in BTO:Er is relatively small, the reduction of lifetime can be attributed to the increased radiative rate.

Unlike chemical methods, the proposed active modulation based on the electric field enables flexible modulating the upconversion PL in a dynamic and reversible manner. Figure 2F shows the transient response of upconversion PL when applying a square voltage ($\sim$2 V @ 20 Hz) to the device. The applied voltage is smaller than the measured coercive voltage. BTO:Er film exhibits switching speed endowed with a rise time of 1.9 ms and a decay time of 2.5 ms, which is two orders of magnitude faster than that of recently reported molecular-assisted
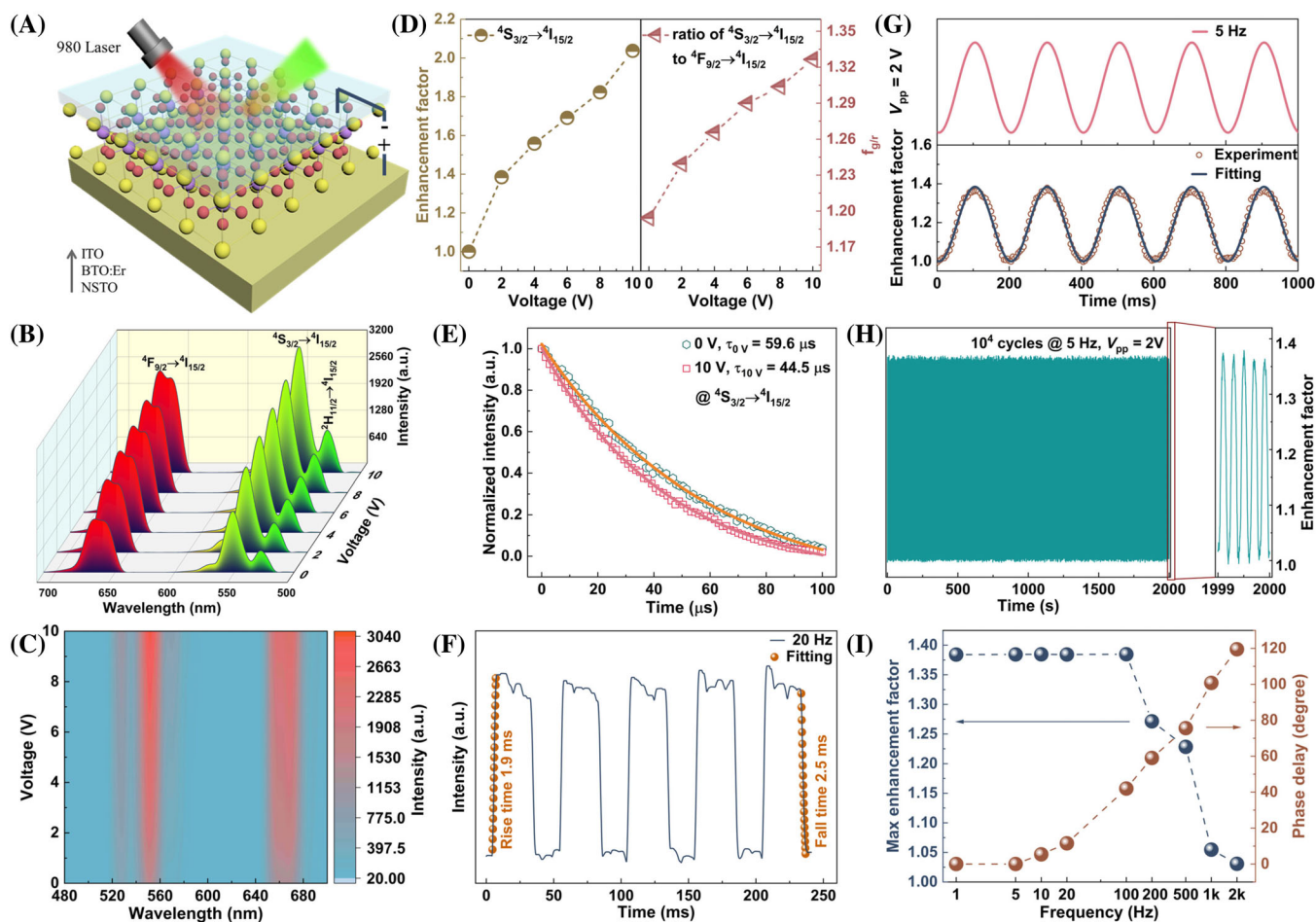
FIGURE 2 Electric field-induced enhancement and modulation of upconversion photoluminescence (PL) in epitaxial BTO:Er thin films. (A) Schematic of the experimental setup. A 980 nm diode laser is chosen as an excitation source. (B) The upconversion PL spectra of BTO:Er thin film under DC bias voltage ranging from 0 to 10 V. (C) Contour map of bias voltage-dependent PL spectra. (D) The enhancement factors for green and red emissions as a function of the applied DC voltage (left axis), and the PL intensity ratio of green to red emission ($f_{g/r}$) (right axis). (E) PL decay curves for the $^4S_{3/2}-^4I_{15/2}$ transition of Er^{3+} ion versus the applied DC voltage, 0 V (yellow) and 10 V (red). (F) Reversible tuning the upconversion emission, recorded at a wavelength of 551 nm, under alternating applied potential (0 and 2 V) at a frequency of 20 Hz. The brown scatter shows the rise time as well as fall time by exponential fitting. (G) The enhancement factor at a wavelength of 551 nm (brown circle scatter) as a function of time while a sinusoidal AC electric voltage (pink solid line) at a frequency of 5 Hz is applied onto the ITO/(BTO:Er)/NSTO heterostructure. The calculated enhancement factor (derived from measured PL intensity) is fitted by $A_0 + A_1 * \sin(\omega t + \varphi)$ as depicted by the dark blue solid line. (H) Cyclic test demonstrates the stability of the dynamic modulation of PL by applying sinusoidal waves (~2 V @ 5 Hz for 10^4 cycles). (I) Frequency-dependent maximum enhancement factor and phase delay of PL intensity at a wavelength of 551 nm.

opto-electrochemical modulation.[32] Given that the energy consumption is one of the key performance metrics of a modulator, which is usually expressed through the energy to switch states. In our case, the calculated switching power of the device is around 140 pJ, which is comparable to the results in the previous studies.[38,39] Figure 2G demonstrates the kinetics of emission intensity at 551 nm in response to a sinusoidal AC bias (~2 V @ 5 Hz). The cyclic test in Figure 2H demonstrates the stability of the dynamic modulation of PL by applying sinusoidal waves (~2 V @ 5 Hz for 10^4 cycles). The PL intensity is synchronously modulated with the applied

sinusoidal voltage. Next, the modulation frequency was increased up to 2000 Hz to investigate the temporal response of the electric-induced modulation. Figure S7 shows the dynamic modulation of PL by applying sinusoidal waves (from 20 to 2000 Hz), with fixed voltage amplitude of 2 V. It can be found that the active modulation can be well preserved up to 100 Hz. With further increasing the frequency, the electrical modulation effect begins to decrease. Until 2000 Hz, the dynamic modulation still can be recognized with an enhancement factor of 1.03. Moreover, notable phase delays between the input electrical trigger and the output PL response

emerge along with the increasing frequency. Figure 2I shows the modulation amplitude and lag phase versus the frequency of the applied electric field. It can be found that with increasing the frequency, the electrical modulation effect fades away, and the lag phases become larger gradually. The modulation speed of ~2000 Hz lags far behind current commercial modulators. But, the lanthanide-based modulators deliver frequency conversion and signal amplification capabilities. The modulation time of millisecond can meet the requirement for visual perception scenarios such as display and image array refreshing.

Upon an electric field applied along the c-axis (perpendicular to the electrode plane), O^{2-} anions shift toward the anode, while Ba^{2+}, Ti^{4+}, and Er^{3+} cations displace to the cathode. The perovskite lattice elongates along the c-axis, and becomes more polarized from these relative displacements (Figure S8). Moreover, the electric field-driven migration of oxygen vacancies is also responsible for PL switching behavior under DC and AC voltages. For Er^{3+}-doped BTO with B-site substitution, extrinsic oxygen vacancies are generated as the principal charge compensating defects to maintain the charge neutrality. As shown in Figure 3A, in response to positive
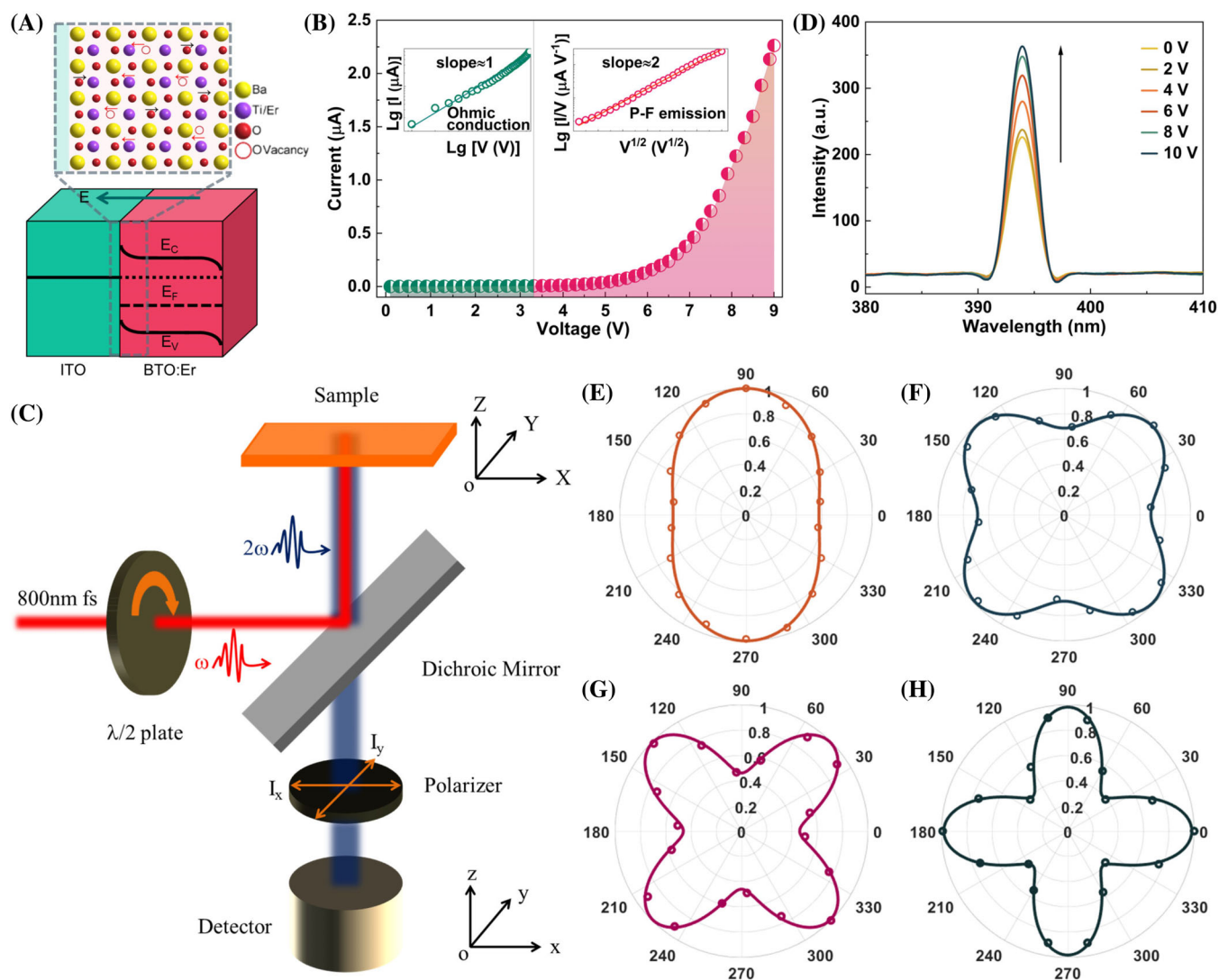

FIGURE 3 Energy band profile at the interface and SHG measurements from the pristine BTO:Er film and the film under external electric field. (A) Schematic band diagram at the ITO/BTO:Er interface under the DC bias. The enlarged area selected from the interface of ITO/BTO:Er elucidates the electric field-induced ionic displacements. (B) I–V curve under forward bias voltage. Insets show the fitted curves. (C) Scheme for SHG measurements. (D) SHG measurements of BTO:Er thin film under various DC bias without the polarizer. (E,F) SHG polar plots measured as a function of incident beam polarization for pristine BTO:Er thin film with the polarizer along the I_x or I_y orientation, respectively. (G,H) SHG polar plots measured as a function of incident beam polarization for pristine BTO:Er thin film under 10 V voltage, with the polarizer along the I_x or I_y orientation, respectively.

electric field (i.e., the electric field points toward ITO), oxygen vacancies with positive charge drift to the cathode. Oxygen vacancy accumulation at the ITO/BTO:Er interface could narrow the depletion layer and lower the Schottky barrier height, which can be verified by the current–voltage (*I–V*) measurement. Since the bandgaps and electron affinities of BTO and NSTO are almost the same (i.e., 3.2 and 3.9 eV, respectively), the Schottky barrier at the interface of BTO:Er/NSTO can be neglected. Therefore, the rectifying characteristic of *I–V* curve in Figure 3B can be ascribed to the Schottky barrier formed at the ITO/BTO:Er interface. In the low bias regime (0–3.2 V), the current increases linearly with the voltage, as indicated by the slope of ∼1 in the lg *I* – lg *V* plot, implying Ohmic conduction. In the high-bias regime (3.3–9.0 V), the slope of 2 in the $\lg(I/V) \sim V^{1/2}$ plot (inset of Figure 3B) reveals Poole–Frenkel (P–F) emission, which involves thermally assisted hopping of electrons from trapped states into the conduction band of the dielectric. We propose that DC bias induces oxygen vacancies accumulation at the ITO/BTO:Er interface, and gives rise to the P–F emission of electrons from these defect states into the conduction band of BTO:Er film.

We further reveal that the excess of oxygen vacancies at the BTO:Er surface leads to the local lattice distortion from tetragonal (*4mm*) symmetry, which plays a crucial role in determining the observed PL responses. Optical second harmonic generation (SHG) is a sensitive tool for detecting broken inversion symmetry.[40] Herein, we examine the structural symmetry changes under different bias conditions by performing in situ SHG polarimetry experiments. Figure 3C shows the experimental setup for the SHG measurements. For convenience, sample axes were set to coincide with the lab axes. Both XRD and TEM confirm that the pristine BTO:Er film consists of tetragonal *a* and *c* domains with the *4mm* point group. The fundamental light propagates parallel along the *c* axis, therefore, *c* domains have no contribution to the observed SHG intensity. The intensity of the output SHG signals was examined at a polarizer angle which is along either parallel (I_x) or perpendicular (I_y) direction as shown in Figure 3C. By fitting the azimuth-polarization-dependent SHG signals (including I_x and I_y) with the theoretical calculation, the experimental polar plots shown in Figure 3E,F indicate that the unbiased pristine BTO:Er film is in the tetragonal *4mm* point group, which is consistent with XRD and TEM observations. Next, we perform in-situ SHG measurement when applying an electric field (along the *c* axis) to the sample. With increasing the electric field, *a* domains will shrink while *c* domains will grow. In that case, the SHG intensity is supposed to decrease with electric field and gradually vanishes. Surprisingly, increasing SHG intensities

were observed from ITO/BTO:Er interface at increasing DC voltages (Figure 3D), with the polarizer absent in the SHG measurement configuration. Such results indicate that the accumulation of oxygen vacancies in the structural framework of BTO results in the formation of new metastable symmetries, as consolidated by previous investigations.[35,41] Extrinsic oxygen vacancies are generally accompanied with partial reduction of Ti^{4+} to Ti^{3+} for charge compensation. Consequently, Ti^{4+}/Ti^{3+} are located in the oxygen-deficient octahedron, resulting in a rhombohedral superlattice with *P3m*1 space group.[42] The azimuth-polarization-dependent SHG results in Figure 3G,H shows that BTO:Er film under 10 V bias belongs to the *3m* point group symmetry. It validates that the electric field-induced accumulation of oxygen vacancies leads to the breaking from tetragonal (*4mm*) symmetry. The SHG intensity in Figure 3D increases with DC bias, indicating that the symmetry deviation degree becomes larger. According to Judd–Ofelt theory, the crystal field effect on the lanthanide dopant can be regarded as the first-order perturbation to the matrix elements of the electric dipole operator. Lower symmetry around the lanthanide dopant means that more uneven crystal-field components can mix opposite-parity into 4f configurations and subsequently increases the electric dipole transition probabilities. Thus, the observed PL enhancement can be ascribed to the distortion of the crystal structure associated with the cations, anions, and oxygen vacancies in the ferroelectric lattice deviated along or against the direction of the electric field. It should be pointed out that such hypothesis is consistent with the observed temporal responses of dynamic modulations. The electric field-induced migration and redistribution of ions and oxygen vacancies is actually a time-dependent process, which inevitably causes a phase lag and determines the cut-off frequency for the active modulation. In a sense, the consequence of the electric field-induced symmetry variation in a single ferroelectric host is in analogy to that of changing host material by conventional chemical methods. Our electrically controllable approach unambiguously provides new opportunities to develop integrated optoelectronic devices.

2.3 | Digital signal encoding

These unique electrically responsive properties endow lanthanide-doped ferroelectric films with great potential in developing multifunctional optoelectronic devices. The possibility to reversibly modulate the PL intensity in proportion to the bias voltage allows to locally encode digital information into visible light signals. As a proof-of-concept, Roman letters "NKU" were optically encoded with

standard eight-bit ASCII code, where "N", "K", and "U" can be conveyed by "01001110", "01001011", and "01010101", respectively. Each letter can be decomposed into 8 binary codes, in which the representing binary codes "0" and "1" correspond to 0 and 9 V electrical bias, respectively. Since the observed PL intensity is associated with the bias voltage, we introduced the enhanced rate $\Delta R = (I_t - I_0)/I_0 \times 100\%$, where I_0 and I_t are the initial emission intensity and the intensity upon electric bias at 551 nm. Using the enhance rate ΔR as optical outputs, we set threshold values of 20% and 70% to define codes "0" and "1" (0, when $\Delta R < 20\%$; 1, when $\Delta R > 70\%$), respectively (Figure 4A). In Figure 4B,C, the electrical information "NKU" was transmitted into optical signals by monitoring the PL intensity. The results indicate that the electric control of PL intensity in BTO:Er film perform superior stability and repeatability. We can further set threshold values of enhance rates corresponding to four binary digits (00, when $\Delta R < 10\%$; 01, when $10\% < \Delta R < 45\%$; 10, when $45\% < \Delta R < 70\%$; 11, when $70\% < \Delta R$), respectively (Figure 4D). And each threshold value is elaborately associated with its bias voltage. As shown in Figure 4E,F, for each letter, eight-bit ASCII characters can be represented by only four optical signals, doubling the data-transfer rate. So the multilevel PL

tunability is in favor of data compression and transmission. Here, we have demonstrated that we can arbitrarily transfer digital information signals into visible luminescent waveforms. Furthermore, such technology furthermore offers a handle on visualization of logic and arithmetic operations as shown in Figures S9–S12, which offer the possibility to develop photonic devices with optical readouts.

2.4 | Logic computing

Besides visualizing digital information signals as mentioned above, the ferroelectric BTO:Er films functionalized with lanthanide emitting centers can be used to construct opto-electronic logic gates. We tackle the design of logic AND and OR gates with the electric voltage and the excitation light intensity as logical inputs and the emission intensity as the logical output. Figure 5A shows the diagram of the logic AND gate and the corresponding truth table. For the implementation of the logic AND gate, we exploit the 980 nm pumping intensity as the optical input (In1). Beam intensities of 1.0 and 1.8 W, corresponding to 79.5 and 143.2 mW mm^{-2}, present the logic values 0 and 1, respectively.
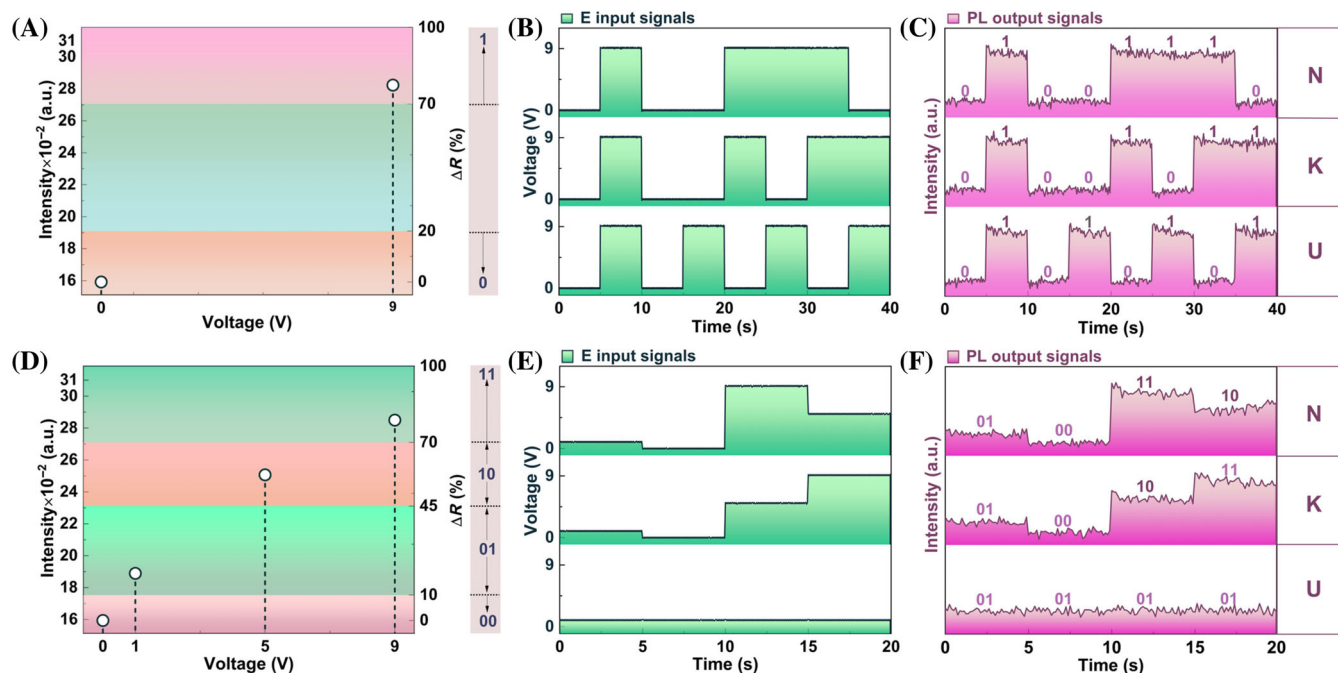

FIGURE 4 Digital encoding based on the electrically modulated upconversion PL at ITO/BTO:Er/NSTO platform. (A) The enhanced rate ΔR of the BTO:Er thin film at 551 nm below the 20% or above the 70% threshold represents binary codes, "0" or "1", respectively. (B,C) Binary information processing of converting electrical inputs which carry the word "NKU" into optical signals. (D) The enhanced rate ΔR below the 10%, between the 10% and 45%, amid the 45% and 70%, or above the 70% threshold represents quaternary codes, "00", "01", "10", or "11", respectively. (E,F) Quaternary information processing of converting electrical inputs which carry the word "NKU" into optical signals.
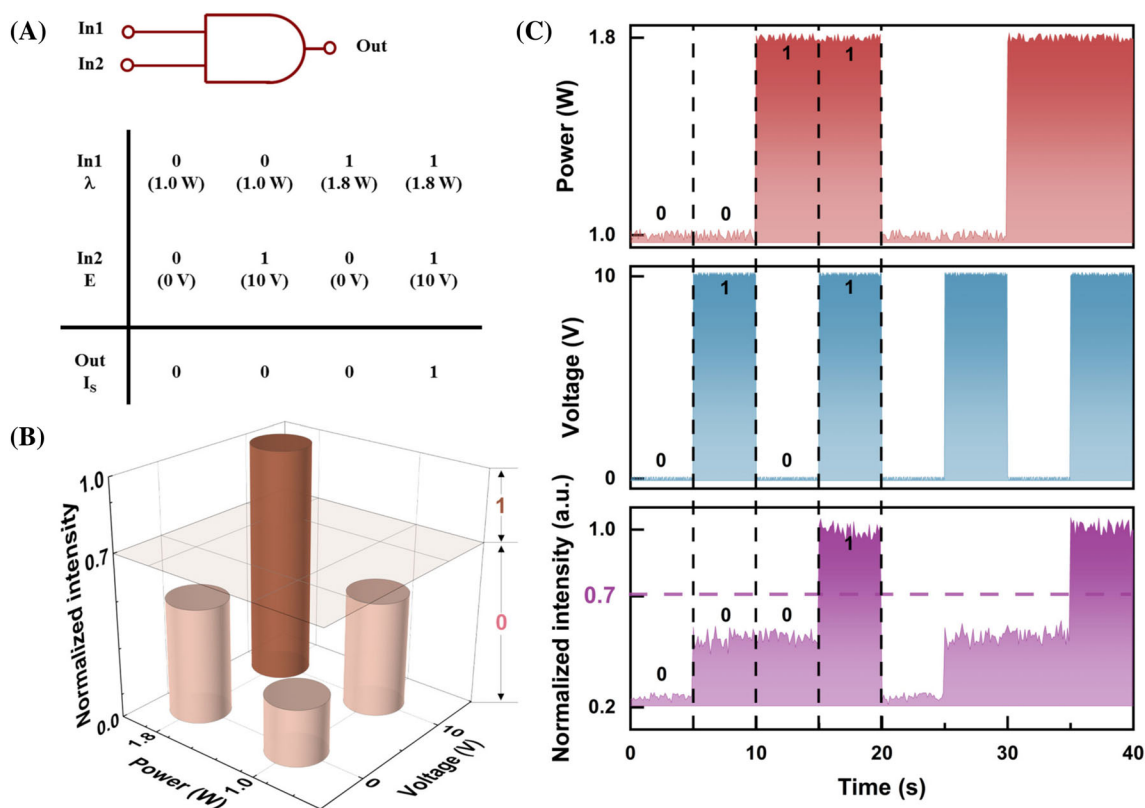
FIGURE 5 Working principle and demonstrations of reconfigurable logic AND gate via photonic readout. (A) Diagram and operating principle of logic AND gate. (B) 3D bar plot of the normalized emission intensity at 551 nm of the BTO:Er thin film displaying a transfer function of logic AND gate. The normalized intensity below the 0.7 or above the 0.7 threshold represents binary codes, "0" or "1", respectively. (C) Dynamic demonstration of the logic AND gate. The input electric voltage and excitation light are set to the same operating frequency, the expected logic outputs are synchronously extracted.

Electric voltage is considered as the electrical input (In2). Voltages (0 or 10 V) define the logic values (0 or 1). PL intensity at 551 nm is used as the logic output. Figure 5B shows the schematic illustration of the AND gate operating principle. Four individual intensities are generated under four different combined conditions. All intensities are normalized to the intensity under pump intensity of 1.8 W in the presence of 10 V bias voltage. And we set a threshold value of 0.7 to define the logic out TRUE (1), or FALSE (0) when the normalized value is below 0.7. Thus, 3D bar plot of the normalized emission intensity at 551 nm of the BTO:Er thin film displays the transfer function of logic AND gate. We also analyze the dynamical behavior of the logic gate. Both the input electric voltage and excitation light were set to the synchronous operating frequency. Figure 5C shows the dynamic demonstration of the logic AND gate, in which the expected logic outputs are synchronously extracted. Analogously, one can also realize a logic OR function by adjusting hybrid optical and electrical inputs as well as the threshold value. Figure S13 shows the demonstration of logic OR gate. Thus, by controlling the excitation beam and

voltage, this enables an implementation of logic functions (such as AND and OR) based on the lanthanide-doped ferroelectric systems.

3 | CONCLUSION

In summary, we have demonstrated a frequency converting and digital modulation of the light derived from the lanthanide-doped ferroelectric films. This combination allows the use of relatively low voltage to engineer the light emission properties on demand without degradation over the consecutive electrical operation. The operation speed can reach up to 2000 Hz, which is orders of magnitude faster than those of photochromic or opto-electrochemical modulations.[43,44] The PL enhancement in thin-film structures under DC voltages arises from the crystal field variation associated with the electric field-driven structural distortion. Moreover, the ability to locally manipulate PL emission enables us to convert digital information-encoded electric signals into visible waveforms, and visualize electrical logic and arithmetic operations. It also allows the

implementation of logic AND or OR function with an expected operation rate up to kHz.

Applications of light modulators are already widespread in optical communication, information storage and processing, Q-switching of lasers, and displays. Commercially available optical modulators (such as electro-optic, magneto-optic, and acousto-optic modulators) manipulate the transmission of light via varying the optical susceptibility of the modulator materials, but no light amplification can be delivered. The demands of versatile optical modulation are still significant. In this work, modulators employing lanthanide emitters have been demonstrated and are arguably the complementary for the traditional devices. The lanthanide family has offered ideal platforms for nonlinear frequency conversion endowed with a gorgeous spectrum. Thus, designed regions of the working frequency spectrum can be accessible through choosing suitable lanthanide dopants, so as to get rid of the frequency limitation that exists in traditional modulators. Considering that light enables high bandwidth, small time-delay, low crosstalk, and power consumption, there are many applications that will benefit from the success of dynamic modulating lanthanide luminescence, including optical interconnects, on-chip integrated microlasers, and optoelectronic synaptic devices.

4 | EXPERIMENTAL SECTION

4.1 | Film growth and device fabrication

Commercial 5×5 mm^2 (001)-oriented 0.7 wt% Nb-doped SrTiO$_3$ (NSTO) single crystals (KJMTI) with a typical resistivity of 0.07 Ω cm were used as the substrates. The BTO:Er polycrystalline target (BaTi$_{0.99}$Er$_{0.01}$O$_{3-\delta}$) was prepared by sintering a mixture of stoichiometric amounts of analytical grade BaCO$_3$, TiO$_2$, and Er$_2$O$_3$ (Aladdin, 99.99%) at 1350°C for 4 h, with two intermediate grinding and pelletizing steps. The BTO:Er film was grown by pulsed laser deposition using a 248 nm KrF excimer laser (Coherent 205F), with the following fabrication parameters: laser energy of 1.5 J cm^{-2}, pulse repetition rate of 2 Hz, substrate temperature of 700°C, and O$_2$ pressure of 20 Pa. The thickness of the as-grown BTO:Er film was measured to be 72 nm. After the deposition, the heterostructure was in situ post-annealed at the growth temperature in 0.5 atmosphere oxygen pressure for 30 min before naturally cooling down to room temperature. A 200-nm thick ITO layer as a top transparent electrode was deposited on the BTO:Er film via pulsed laser deposition by following conditions: growth temperature of 250°C, oxygen pressure of 2.5 Pa, a laser fluence of 1.2 J cm^{-2}, and a repetition rate of 2 Hz.

4.2 | Material characterizations and photoresponse measurements

The x-ray diffractometer (Bruker D8 Discover: $\lambda = 1.5406$ Å, Cu Kα1 radiation) was used to investigate the crystal structure of the samples. AFM and PFM measurements were conducted using the Asylum Research MFP-3D Infinity (Oxford Instrument). The cross-sectional TEM samples were prepared using a dual-beam focused-ion-beam scanning electron microscopy system (FEI Helios G4 UX). The STEM images were collected by an aberration-corrected Thermo Fisher Spectra 300 STEM. SHG testing was performed by an Olympus FV300 confocal microscope coupled with an 800 nm Coherent Mira 900 laser. The x-ray photoelectron spectroscopy (XPS) measurements were taken using a ThermoFisher Scientific ESCALAB 250Xi instrument. The PL spectra were recorded using a SpectraPro 300i spectrophotometer under the excitation of a 980 nm diode laser. The transient decay curve was recorded using a photomultiplier tube (H11902-04, Hamamatsu) coupled with a Rigol DS2202E digital oscilloscope. The I–V curve was measured with a Keithley 6430 SourceMeter. The alternating signals were produced with a Rigol DG4202 Arbitrary Waveform Generator. All measurements were conducted at room ambient temperature.

4.3 | Second harmonic generation calculations

Pristine BTO:Er thin film grown on the NSTO (100) substrate consists of tetragonal a and c domains with the *4mm* point group. For simplicity, sample axes (X,Y,Z) coincide with the lab axes (x, y, z). The electric components of the fundamental light can be described as $E^\omega(\varphi) = (E_1, E_2, E_3) = (-E_0\sin\varphi, 0, \pm E_0\cos\varphi)$, where φ is the azimuthal angle of the fundamental light polarization as seen in Figure 3C. The light-induced nonlinear polarization originated from in-plane polarized domains can be calculated using the SHG tensor of *4mm* point group:

$$P^{2\omega} = \begin{pmatrix} P_1 \\ P_2 \\ P_3 \end{pmatrix} = \begin{pmatrix} 0 & 0 & 0 & 0 & d_{15} & 0 \\ 0 & 0 & 0 & d_{15} & 0 & 0 \\ d_{31} & d_{31} & d_{33} & 0 & 0 & 0 \end{pmatrix} \begin{pmatrix} E_1^2 \\ E_2^2 \\ E_3^2 \\ 2E_2E_3 \\ 2E_1E_3 \\ 2E_1E_2 \end{pmatrix}.$$

The measured polarizer is placed either parallel (I_x) or perpendicular (I_y), the output SHG intensity

can be expressed as $I_x^{2\omega} = I_{X_3}^{2\omega} \propto \left(P^{2\omega} \cdot A_x\right)^2 = \left(d_{33}E_0^2\cos^2\varphi + d_{31}E_0^2\sin^2\varphi\right)^2$, and $I_y^{2\omega} = I_{X_1}^{2\omega} \propto \left(P^{2\omega} \cdot A_y\right)^2 = \left(d_{15}E_0^2\sin 2\varphi\right)^2$, where $A_x = (0,0,1)$, $A_y = (1,0,0)$. As shown in Figure 3E,F, the experimental polar plots match the *4mm* point group-based SHG expressions well, indicating that the pristine BTO:Er is in the tetragonal *4mm* point group. When 10 V voltage is applied across the BTO:Er thin film, the transformation from the tetragonal (*4mm*) to the trigonal (*3m*) occurs. Via appropriately rotating the sample, the crystal physics axes (X_1, X_2, X_3) can coincide with the lab axes (x, y, z). The electric field of the fundamental beam has components $E^\omega(\varphi) = (-E_0\cos\varphi, -E_0\sin\varphi, 0)$, which induces a nonlinear polarization of:

$$
P^{2\omega} = \begin{pmatrix} P_1 \\ P_2 \\ P_3 \end{pmatrix}
$$

$$
= \begin{pmatrix} 0 & 0 & 0 & 0 & d_{15} & -d_{22} \\ -d_{22} & d_{22} & 0 & d_{15} & 0 & 0 \\ d_{31} & d_{31} & d_{33} & 0 & 0 & 0 \end{pmatrix} \begin{pmatrix} E_1^2 \\ E_2^2 \\ E_3^2 \\ 2E_2E_3 \\ 2E_1E_3 \\ 2E_1E_2 \end{pmatrix}
$$

$$
= \begin{pmatrix} -d_{22}E_0^2\sin 2\varphi \\ -d_{22}E_0^2\cos 2\varphi \\ d_{31}E_0^2 \end{pmatrix}.
$$

The SHG polar plots are $I_x^{2\omega}(\varphi) \propto \left(P^{2\omega}(\varphi) \cdot A_x\right)^2 = \left(d_{22}E_0^2\sin 2\varphi\right)^2$, $I_y^{2\omega}(\varphi) \propto \left(P^{2\omega}(\varphi) \cdot A_y\right)^2 = \left(d_{22}E_0^2\cos 2\varphi\right)^2$, where $A_x = (0,0,1)$, $A_y = (1,0,0)$. The SHG plots in Figure 3G,H fit well with the calculated plots, indicating the symmetry of *3m* point group in the biased BTO:Er thin film.

ACKNOWLEDGMENTS

CONFLICT OF INTEREST STATEMENT

The authors declare no conflict of interest.

ORCID

Yang Zhang https://orcid.org/0000-0002-9840-1755
Jianhua Hao https://orcid.org/0000-0002-6186-5169

REFERENCES

1. Reed GT, Mashanovich G, Gardes FY, Thomson DJ. Silicon optical modulators. *Nat Photon*. 2010;4(8):518-526.
2. Eltes F, Villarreal-Garcia GE, Caimi D, et al. An integrated optical modulator operating at cryogenic temperatures. *Nat Mater*. 2020;19(11):1164-1168.
3. Xu M, Zhu Y, Pittalà F, et al. Dual-polarization thin-film lithium niobate in-phase quadrature modulators for terabit-per-second transmission. *Optica*. 2022;9(1):61-62.
4. Wilson J, Hawkes JF. *Optoelectronics: An Introduction*. Prentice Hall; 1989.
5. Wang T, Zhang D, Yang S, et al. Magnetically-dressed CrSBr exciton-polaritons in ultrastrong coupling regime. *Nat Commun*. 2023;14(1):5966.
6. Li GL, Yu PKL. Optical intensity modulators for digital and analog applications. *J Light Technol*. 2003;21(9):2010-2030.
7. Feldmann J, Youngblood N, Wright CD, Bhaskaran H, Pernice WHP. All-optical spiking neurosynaptic networks with self-learning capabilities. *Nature*. 2019;569(7755):208-214.
8. El Srouji L, Krishnan A, Ravichandran R, et al. Photonic and optoelectronic neuromorphic computing. *APL Photonics*. 2022; 7(5):051101.
9. Powell K, Li L, Shams-Ansari A, et al. Integrated silicon carbide electro-optic modulator. *Nat Commun*. 2022;13(1):1851.
10. Imbrock J, Wesemann L, Kroesen S, Ayoub M, Denz C. Waveguide-integrated three-dimensional quasi-phase-matching structures. *Optica*. 2020;7(1):28-34.
11. Halasyamani PS, Rondinelli JM. The must-have and nice-to-have experimental and computational requirements for functional frequency doubling deep-UV crystals. *Nat Commun*. 2018;9(1):2972.
12. Kang L, Lin Z. Deep-ultraviolet nonlinear optical crystals: concept development and materials discovery. *Light Sci Appl*. 2022; 11(1):201.
13. Zhou B, Shi B, Jin D, Liu X. Controlling upconversion nanocrystals for emerging applications. *Nat Nanotechnol*. 2015; 10(11):924-936.
14. Chen S, Weitemier AZ, Zeng X, et al. Near-infrared deep brain stimulation via upconversion nanoparticle-mediated optogenetics. *Science*. 2018;359(6376):679-684.
15. Jin L, Chen X, Wu Y, et al. Dual-wavelength switchable single-mode lasing from a lanthanide-doped resonator. *Nat Commun*. 2022;13(1):1727.
16. Xie Y, Song Y, Sun G, Hu P, Bednarkiewicz A, Sun L. Lanthanide-doped heterostructured nanocomposites toward advanced optical anti-counterfeiting and information storage. *Light Sci Appl*. 2022;11(1):150.
17. Yang D, Pa M, Hou Z, Cheng Z, Li C, Lin J. Current advances in lanthanide ion (Ln^{3+})-based upconversion nanomaterials for drug delivery. *Chem Soc Rev*. 2015;44(6):1416-1448.
18. Clausen C, Usmani I, Bussières F, et al. Quantum storage of photonic entanglement in a crystal. *Nature*. 2011;469(7331): 508-511.

19. Werts MHV. Making sense of lanthanide luminescence. *Sci Prog.* 2005;88(2):101-131.

20. Zhai Y, Zhou Y, Yang X, et al. Near infrared neuromorphic computing via upconversion-mediated optogenetics. *Nano Energy.* 2020;67:104262.

21. Xie Y, Sun G, Mandl GA, et al. Upconversion luminescence through cooperative and energy-transfer mechanisms in Yb^{3+}-metal-organic frameworks. *Angew Chem Int Ed.* 2023;62(4):e202216269.

22. Zhai Y, Yang X, Wang F, et al. Infrared-sensitive memory based on direct-grown MoS_2-upconversion-nanoparticle heterostructure. *Adv Mater.* 2018;30(49):1803563.

23. Zhong M, Hedges MP, Ahlefeldt RL, et al. Optically address-able nuclear spins in a solid with a six-hour coherence time. *Nature.* 2015;517(7533):177-180.

24. Ma Y, Ma Y-Z, Zhou Z-Q, Li C-F, Guo G-C. One-hour coherent optical storage in an atomic frequency comb memory. *Nat Commun.* 2021;12(1):2381.

25. Deng R, Qin F, Chen R, Huang W, Hong M, Liu X. Temporal full-colour tuning through non-steady-state upconversion. *Nat Nanotechnol.* 2015;10(3):237-242.

26. Lei L, Wang Y, Xu W, et al. Manipulation of time-dependent multicolour evolution of X-ray excited afterglow in lanthanide-doped fluoride nanoparticles. *Nat Commun.* 2022;13(1):5739.

27. Wisser MD, Chea M, Lin Y, et al. Strain-induced modification of optical selection rules in lanthanide-based upconverting nanoparticles. *Nano Lett.* 2015;15(3):1891-1897.

28. Dong Z, Chen H, Qi M, et al. Enhanced upconversion photoluminescence assisted by flexoelectric field in oxide nanomembranes. *Laser Photonics Rev.* 2022;16(4):2100454.

29. Chen H, Shen J, Du X, et al. In situ probing the heating effect and phase transition in perovskite heterostructures. *Mater Des.* 2023;232:112093.

30. Wang F, Liu X. Multicolor tuning of lanthanide-doped nanoparticles by single wavelength excitation. *Acc Chem Res.* 2014;47(4):1378-1385.

31. Ye S, Teng Y, Juan A, Wei J, Wang L, Guo J. Modulated visible light upconversion for luminescence patterns in liquid crystal polymer networks loaded with upconverting nanoparticles. *Adv Opt Mater.* 2017;5(4):1600956.

32. Wu Y, Xu J, Qin X, Xu J, Liu X. Dynamic upconversion multicolour editing enabled by molecule-assisted opto-electrochemical modulation. *Nat Commun.* 2021;12(1):2022.

33. Zhang Y, Jie W, Chen P, Liu W, Hao J. Ferroelectric and piezo-electric effects on the optical process in advanced materials and devices. *Adv Mater.* 2018;30(34):1707007.

34. Yi X, Shang J, Pan L, et al. Reversible luminescence modula-tion upon an electric field on a full solid-state device based on lanthanide dimers. *ACS Appl Mater Interfaces.* 2016;8(24):15551-15556.

35. Ascienzo D, Kurt O, Greenbaum S, et al. Local structural changes due to the electric field-induced migration of oxygen vacancies at Fe-doped $SrTiO_3$ interfaces. *J Am Ceram Soc.* 2019;102(7):4353-4366.

36. Hao J, Zhang Y, Wei X. Electric-induced enhancement and modulation of upconversion photoluminescence in epitaxial $BaTiO_3$:Yb/Er thin films. *Angew Chem Int Ed.* 2011;50(30):6876-6880.

37. Ma Y, Yang S, Zhao C, et al. Photochromic and electric field-regulating luminescence in high-transparent (K,Na)NbO_3-based ferroelectric ceramics with two-phase coexistence. *ACS Appl Mater Interfaces.* 2022;14(31):35940-35948.

38. Li C, Hu M, Li Y, et al. Analogue signal and image processing with large memristor crossbars. *Nat Electron.* 2018;1(1):52-59.

39. Cheng Z, Ríos C, Youngblood N, Wright CD, Pernice WHP, Bhaskaran H. Device-level photonic memories and logic appli-cations using phase-change materials. *Adv Mater.* 2018;30(32):1802435.

40. Denev SA, Lummen TTA, Barnes E, Kumar A, Gopalan V. Probing ferroelectrics using optical second harmonic genera-tion. *J Am Ceram Soc.* 2011;94(9):2699-2727.

41. Park D-S, Hadad M, Riemer LM, et al. Induced giant piezoelec-tricity in centrosymmetric oxides. *Science.* 2022;375(6581):653-657.

42. Woodward DI, Reaney IM, Yang GY, Dickey EC, Randall CA. Vacancy ordering in reduced barium titanate. *Appl Phys Lett.* 2004;84(23):4650-4652.

43. Gong J, Du P, Li W, Yuan G, Mao X, Luo L. The enhancement of photochromism and luminescence modulation properties of ferroelectric ceramics via chemical and physical strategies. *Laser Photonics Rev.* 2022;16(10):2200170.

44. Hernández-Rodríguez MA, Brites CDS, Antorrena G, et al. Lanthanide luminescence to mimic molecular logic and com-puting through physical inputs. *Adv Opt Mater.* 2020;8(12):2000312.

SUPPORTING INFORMATION

Additional supporting information can be found online in the Supporting Information section at the end of this article.